A Closed-loop PMSM Sensorless Control Based-on the Machine Acoustic Noise

Amirhossein Malekipour, Adrien Corne, Lauric Garbuio, Pierre Granjon, Laurent Gerbaud

A Closed-loop PMSM Sensorless Control Based-on the Machine Acoustic Noise

Amirhossein Malekipour, *IEEE Graduate Student Member*, Adrien Corne, *IEEE Member*, Lauric Garbuio, *IEEE Member* , Pierre Granjon, and Laurent Gerbaud, *IEEE Member*

***Abstract*—In this paper, a novel sensorless control for Permanent Magnet Synchronous Machine (PMSM) using its radiated acoustic noise is proposed in which a high-frequency voltage signal is superimposed upon the fundamental excitation and the machine response to such excitation is studied. Firstly, the analytical equations describing the field formation within the airgap leading to the generation of radial forces and acoustic noise are extensively investigated. In the next step, resulting harmonics in the acoustic noise waveform caused by the injected signals are predicted. Then it is experimentally verified that, depending on the machine structure, there will be some distinctive sidebands around the injected frequency directly related to the fundamental synchronous frequency. Acoustic noise waveform is highly distorted and sensitive to the environment, so a proposed 4-stage signal processing algorithm containing two self-adaptive Band-pass Filters (BPF) are used to safeguard the signal against unwanted distortions and flawlessly extract the rotor position information. Robustness and effectivity of this method is verified experimentally in various operating conditions.**

***Index Terms*—Acoustic noise, high-frequency injection (HFI), permanent magnet synchronous machine (PMSM), rotor position estimation, signal processing, sensorless control.**

I. Introduction

HAVING a high-performing PMSM is intertwined with knowing the rotor position usually provided by position sensors in the form of encoders or resolvers. Existence of such a sensor not only increases the system overal size and weight, but also amplifies the succeptiblity to fault and conduction noise leading to reliability issues. Consequently, elimination of position sensor dependence in PMSM control, known as sensorless control, has been a burgeoning focal point among academics and industrials since the past few decades.

Although there exists a multitude of sensorless algorithms proposed for PMSM, they can be categorised into two general groups, model-based and saliency-based methods [1]. Considering the PMSM model in the stationary reference frame, back electromotive force (EMF) and its extended version (EEMF) containing rotor position information can be estimated as the basis for the model-based method in the medium-high speed range [2]. Different methods and structures for estimation of rotor position and speed using the EMF and EEMF are extensively investigated in [3]–[8].

Inherent machine inductance variation could also be used as the ground for the saliency-based sensorless algorithm; typically a High-Frequency Injection (HFI) in the form of voltage or current is applied and the system response to this excitation is used as the information source. HFI-based methods can show more effectiveness in zero-low speed range where the EMF is of null or negligible magnitude. In the case of injection in the stationary reference frame called Rotating Voltage Injection Method, a voltage space vector is injected. On the other hand, there is Pulsating Voltage Injection Method where a voltage signal, which can be either sinusoidal or square-wave, is injected in the synchronous reference frame [4], [9]; it is also possible to inject a voltage space vector in the synchronous reference frame to realise the Pulsating Voltage Injection method [10].

A comparison among Pulsating and Rotating Voltage Injection methods implemented on different PMSMs is carried out in [11]. It is shown that by injecting a pulsating voltage signal into an estimated fixed-frequency rotating frame other than the conventional synchronous reference frame, the limited system stability in addition to its long convergence time could be overcome [12]. Moreover, typical Low-pass Filter (LPF)-based signal demodulation stage of the conventional HFI methods leading to marginal stability issues can be replaced by a direct filterless demodulation algorithm [13]. Improving the filtering performance, LPF can be replaced by a Second-order Generalized Integrator (SOGI) acting as a Band-pass Filter (BPF) with tunable parameters [14], [15].

Although the majority of HFI methods process the derived currents to extract rotor position information, it is feasible to use zero-sequence carrier voltage instead [16]. The carrier signal at the switching frequency can also be used to provide rotor position information; compared to the previous HFI methods, this method provides an alleviated acoustic noise and vibration level due to the high frequency of carrier signal [17], [18]. In addition to the current or EMF, the vibration on the surface of stator can also be processed to obtain the magnet polarity for a given PMSM [19].

Acoustic noise, vibration, and harshness (NVH) in variable-speed drives usually stem from three main sources: aerodynamic, mechanical, and electromagnetic with the most contribution especially in medium-speed drives. Electromagnetic forces formed inside the airgap are the fundamental cause for the NVH occurrence; the impact of modern PWM-based control strategies on the NVH waveform and frequency components is of unquestionable importance also [20].

Although NVH aspects of PMSM (studying the occurrence mechanism, analytical system description, methods to allay its amplitude, and NVH-based fault detection) have garnered

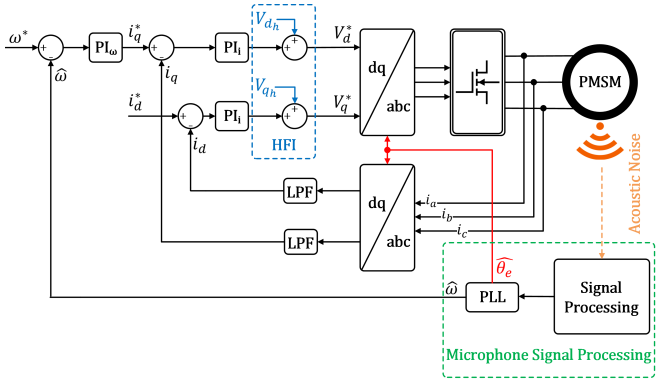

Fig. 1. Overall configuration of an acoustic noise-based sensorless algorithm.

considerable attention over the years, rarely can be found a study concentrated on extraction of information from HFI-induced aspects.

Given the available literature review, almost all sensorless methods are based on EMF or current processing. This paper, on the contrary, proposes a novel method for implentation of a closed-loop PMSM sensorless control using the the extracted rotor position information from the machine radiated acoustic noise with the overall system schematic depicted in Fig. (1).

Utilization of a microphone, instead of an accelerometer, yields an overall system cost reduction found useful for the automotive industry. Besides, the microphone can be an alternative for the faulty position sensor by increasing the system reliability appealing to the more electric aircraft technology. It is also noteworthy that in some cases like acoustic noise-based fault diagnosis, the microphone is already a part of the system and so can be used to replace the position sensor.

The paper is organized as follows; the impact of HFI method on the radiated acoustic noise is extensively investigated in Section II, the procedure for extraction of rotor position information from the captured acoustic noise is presented in Section III, and Section IV experimentally verifies the feasibility of using acoustic noise for sensorless control of a given PMSM in different working conditions.

II. Harmonic Components of Current and Radial Force

Throughout this section, firstly, the general analytical equations governing the radial force formation within the airgap considering the impact of permanent magnets (PM) and armature currents are provided. Then, current harmonics generated as the result of HFI method are derived and finally, the impact of HFI method on the harmonic components of the radial force and accordingly the generated acoustic noise are investigated.

A. Frequency-domain radial force composition

In a PMSM, vibration and acoustic noise occur due to different reasons among which electromagnetic-origined are of higher concern to this study. Radial electromagnetic force formed inside the airgap is the underlying cause for the occurrence of acoustic noise; if one of the radial force frequencies coincides with natural frequencies of the stator structure, high level of acoustic noise and vibration, known as resonance, occurs. Through analytical methods verified with finite element analyses, it is proved that the stator slotting effect and the tangential components of the airgap field have negligible impacts on the radial force waveform [21]. Consequently, given a general format for the phase current shown in (1), a simplified model for the radial airgap field comprising the magnet field in addition to the armature reaction can be presented as follows [22]

$$i_{ph} = \sum_{i=1}^{\infty} I_i.cos\left(iP\omega_m t + \phi_i\right) \tag{1}$$

$$B_{arm} = \sum_{k}^{\infty}\sum_{i=1}^{\infty} b_{arm}\left(r\right).I_i.sin\left[k\theta \pm \left(iP\omega_m t + \phi_i\right)\right] \tag{2}$$

$$B_{PM} = \sum_{j=1,3,5}^{\infty} b_{PM}\left(r\right).cos\left[jP\left(\theta - \omega_m t\right)\right] \tag{3}$$

$$k \pm i = 3C, C = \{0, \pm1, \pm2, \pm4, \pm5, \pm7, \pm8, ...\} \tag{4}$$

where i_{ph}, I_i, P, ω_m, θ, and ϕ_i correspondingly denote the phase current, amplitude of the i^{th} harmonic of the phase current, number of pole pairs, mechanical angular velocity of the rotor, angular position around the stator periphery, and arbitrary initial phase of the i^{th} harmonic in the phase current. Moreover, in a PMSM, phase current harmonics (i) are of specific nontriplen order (1,5,7,11,...), b_{arm} and b_{PM} are constants depending on the stator dimensions, including radius of analysis in the airgap (r), given a two-dimensional cross section of the machine, and C and k are constant values shown in (4) [22].

Maxwell Stress Tensor is the principal method by which the radial force formed in the airgap is derived; for a given PMSM with small slot opening and airgap length, contributation of circumferential forces having magnitudes tens of times smaller than the radial ones can be safely disregarded [23], thus

$$F_{rad} \approx \frac{B_{rad}^2}{2\mu_0} = \frac{1}{2\mu_0}\left[\begin{array}{c}\sum_{k}^{\infty}\sum_{i=1}^{\infty} b_{arm}(r) I_i.sin(k\theta \pm (iP\omega_m t + \phi_i)) \\ + \\ \sum_{j=1,3,5}^{\infty} b_{PM}\left(r\right).cos\left(jP\left(\theta - \omega_m t\right)\right)\end{array}\right]^2 \tag{5}$$

Expanding (5), individual and mutual contributions of the armature reaction and magnet fields to the total radial force, in terms of frequency components, can be concluded as F_{rad}^{arm}, F_{rad}^{PM}, and F_{rad}^{arm+PM} respectively.

$$F_{rad}^{arm} \propto \sum_{k_1}^{\infty}\sum_{k_2}^{\infty}\sum_{i_1=1}^{\infty}\sum_{i_2=1}^{\infty} sin\left(k_1\theta \pm \left(i_1 P\omega_m t + \phi_{i_1}\right)\right) .sin\left(k_2\theta \pm \left(i_2 P\omega_m t + \phi_{i_2}\right)\right) \tag{6}$$

$$F_{rad}^{PM} \propto \sum_{j_1=1,3,5}^{\infty}\sum_{j_2=1,3,5}^{\infty} cos\left(j_1 P\left(\theta - \omega_m t\right)\right).cos(j_2 P(\theta - \omega_m t)) \tag{7}$$

$$F_{rad}^{arm+PM} \propto \sum_{j=1,3,5}^{\infty}\sum_{i=1}^{\infty}\sum_{k}^{\infty} sin\left(k\theta \pm \left(iP\omega_m + \phi_i\right)\right).cos\left(jP\left(\theta - \omega_m t\right)\right) \tag{8}$$

TABLE I
PARAMETERS OF THE STUDIED PMSM.

Parameter	*Value*
No. of Slots/Poles	9/6
Rated Power	$1600W$
Rated Speed	$1500rpm$
d-/q-Axis Inductances	$140\mu H/178\mu H$
Phase Resistance	$97m\Omega$
PM Flux Linkage	$39.5mWb$

Given (6-8), for a PMSM with 6 rotor poles and 9 stator slots with parameters given in Table. I, individual harmonic components of magnet and armature reaction fields can be concluded as

$$\begin{cases} B_{PM} \Rightarrow jPf_m = f_e \times \left\{ \underbrace{1,3,5,7,...}_{j} \right\} \\ B_{arm} \Rightarrow f_{ei} \times \{1,2,4,5,7,8,...\} \end{cases} \tag{9}$$

where f_e is the electrical fundamental frequency and f_{ei} is the apperaed frequency in the current; for the fundamental excitation, $f_{ei} = f_e$. Magnet-related harmonics are only dependent on the number of pole pairs and mechanical revolution speed, thus are always constant regardless of the current harmonics. Armature-related components, however, are directly related to the current harmonics; the mutual impact of fundamental and swithching carrier frequencies upon the radial force and radiated acoustic noise are also extensively investigated in [24]. Given (9), the harmonic components appeared in the radial force taking into account the self and mutual impacts of magnets and armature reaction components can be obtained which is extensively discussed about in the subsection C.

B. Current harmonics considering HFI method

Additional current harmonics generated in HFI methods and their contribution to the aggregated radial force and disseminated acoustic noise are of cardinal importance since they carry vital rotor position information essential for the sensorless control. The voltage equation of PMSM in the stationary reference frame is defined as

$$V_{\alpha\beta} = (r + \rho L_{\alpha\beta})\, i_{\alpha\beta} + \underbrace{\omega_e \psi_m \begin{bmatrix} -sin(\theta_e) \\ cos(\theta_e) \end{bmatrix}}_{EMF} \tag{10}$$

where $V_{\alpha\beta}$, r, ρ, $L_{\alpha\beta}$, $i_{\alpha\beta}$, ψ_m, and θ_e are respectively representing voltage, phase resistance, differential operator, inductance, current, magnet flux, and electrical position in the corresponding reference frame. In case of superimposing, on top of the fundamental component, a sinusoidal voltage with frequency of ω_h at least hundreds of times greater than the fundamental frequency, resistive voltage drop and the EMF terms in (10) could be neglected yielding

$$i_{\alpha\beta} \approx \frac{V_h}{\omega_h L_d L_q} \begin{bmatrix} \Sigma L - \Delta L cos(2\theta_e) & -\Delta L sin(2\theta_e) \\ -\Delta L sin(2\theta_e) & \Sigma L + \Delta L cos(2\theta_e) \end{bmatrix} \int V_{\alpha\beta} dt \tag{11}$$

with $\Sigma L = \frac{L_d + L_q}{2}$, $\Delta L = \frac{L_d - L_q}{2}$, and V_h, L_d, and L_q are correspondingly denoting the amplitude of injected voltage, the direct-, and quadrature-axis inductance. Given a voltage space vector injected in the estimated synchronous frame as

$$V_{dq_h} = jV_h e^{j\omega_h t} = \begin{bmatrix} -V_h sin(\omega_h t) \\ V_h cos(\omega_h t) \end{bmatrix} \tag{12}$$

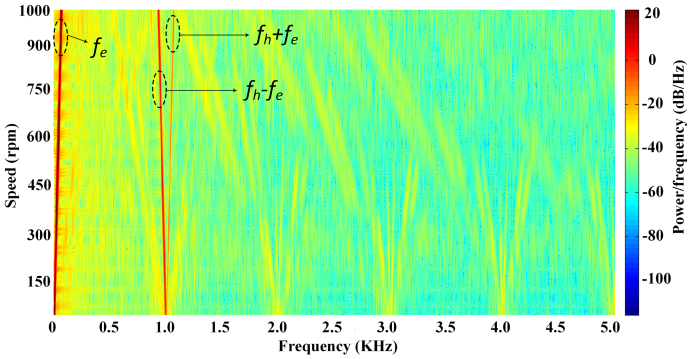

Fig. 2. Current spectrogram for the case of injecting in the estimsted synchronous frame.

and using (11) and knowing that $V_{\alpha\beta} = V_{dq}.e^{j\theta_e}$, current in the stationary reference frame can be obtained as

$$i_{\alpha\beta}^{V_{dq_h}} = \frac{V_h}{\omega_h L_d L_q} \begin{bmatrix} \Sigma L.cos(\omega_h t + \theta_e) - \Delta L.cos(\omega_h t - \theta_e) \\ \Sigma L.sin(\omega_h t + \theta_e) + \Delta L.sin(\omega_h t - \theta_e) \end{bmatrix} \tag{13}$$

which has a pair of symmetrical position-related sideband around the injected frequency ($\omega_h \pm \omega_e$). Figure (2) illustrates the current spectrogram for a generic PMSM running from 0 to $1000rpm$ for the mentioned injection style while the injection frequency is set to $1KHz$. Looking at Fig.(2), three spectral rays conspicuously stand out from the blue-green background, one in the ultra-low frequency range directly representing the fundamental frequency (f_e) and the others around the injected frequency verifying the presented mathematical current derivations shown in (13).

C. Radial force harmonics considering HFI method

Choosing the rotating reference frame for the injection leading to the currents shown in (13) and considering (5-9), the dominant harmonics in the radial force reflecting the harmonics in the acoustic noise are calculated as

$$\begin{cases} F_{rad}^{PM} \Rightarrow f_e \times \left\{ \underbrace{2,4,6,8,...}_{Even} \right\} \\ F_{rad}^{arm} \Rightarrow f_{ei} \times \{1,2,3,4,...\} \\ F_{rad}^{PM+arm} \Rightarrow \underbrace{f_{ei}}_{arm} \pm \underbrace{f_e \times \left\{ \underbrace{1,3,5,7,...}_{Odd} \right\}}_{PM} \end{cases} \tag{14}$$

where $f_{ei} = f_h \pm f_e$. Expected harmonics in the acoustic noise are fallen in three zones; the first one contains low-order harmonics resulted from the magnet field only (F_{rad}^{PM}), the second zone contains harmonics related to the armature reaction spreading over a wide range with steps equal to f_{ei} (F_{rad}^{arm}), and the last and the most important zone, F_{rad}^{PM+arm}, encompasses the mutual impact of armature reaction and magnet fields with harmonic orders defined as $f_h \pm f_e \times \{0,2,4,6,8,...\}$.

Acoustic noise spectrogram for a PMSM with 6 poles and 9 stator slots revolving at $50 - 1000rpm$ with the injected frequency of $f_h = 1440$Hz is depicted in Fig. (3). In full

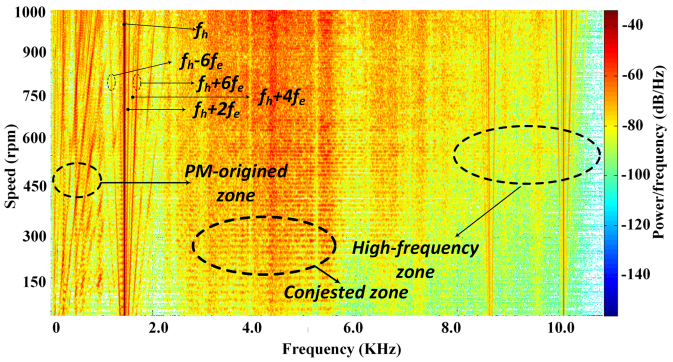

Fig. 3. Acoustic noise spectrogram for the case of injecting in the synchronous reference frame with the frequency of $f_h = 1440$Hz.

congruence with (14), the influence of magnets on the acoustic noise spectra is located in the low-frequency zone indicated by PM-origined zone and the mutual impact of magnets and armature reaction contribting to the most important zone is at the injected frequency in addition to its distinctive sidebands carrying rotor position information. Moreover, there are two other zones in the medium- and high-frequency ranges; the first one is called the congested zone within which numerous random harmonic components exist making this zone almost of no use and the other is called the high-frequency zone containing rotor position information. This zone, however, needs complex filter design and has high susceptibility to noise. As a result, in this paper, sensorless control of PMSM is realised focusing on the vicinity of the injected frequency.

Focusing on the proximity of the injected frequency in Fig. (2) and Fig.(3) and given (13) and (14), one can conclude that there is only one pair of speed-dependant sideband in the current spectra while there are multiple (at least three) pairs of such sidebands existing in the spectra of the machine acoustic noise. Consequently, compared to the current waveform, acoustic noise is a richer source for extracting the rotor position information.

III. Acoustic Noise-Based Sensorless Control of PMSM

A. Signal processing

Acoustic noise spectra of a PMSM is fraught with frequency components only a narrow band of which containing rotor position information is of importance; therefore, accurate extraction of the desired components from the highly-distorted background requires a four-stage scrupulous signal processing algorithm as shown in Fig. (4). Radiated acoustic noise of the machine is firstly captured via a microphone in the $Stage\ I$, then, in order to eliminate the unwanted harmonics and extract the vicinity zone of the injected frequency, a band-pass filter (BPF) is used providing the trimmed waveform in $Stage\ II$. This stage is then followed by a vectorized demodulation to shift the components by $\pm f_h$ $(StageIII)$ prior to the final band-pass filtering extracting the desired harmonics of the electrical frequency in $Stage\ IV$ (the frequency components in each processing stage are summarized in Table II).

It is worth mentioning that having a complex demodulation scheme is indispensable since a pair of orthogonal signals

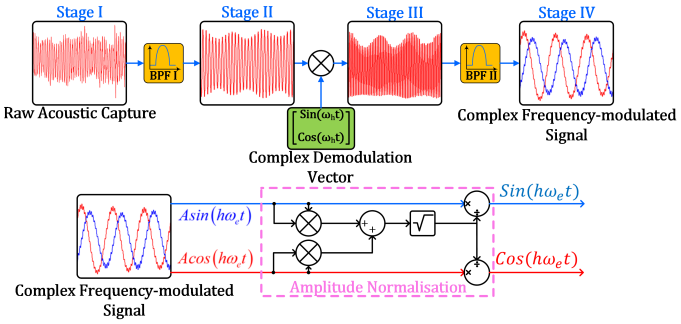

Fig. 4. Acoustic noise signal processing stages for the extraction of signals containing rotor position information.

TABLE II
FREQUENCY COMPONENT VARIATION IN EACH OF THE STAGES.

Stage	*Frequency Components*
Stage I	$\sum_{n=1}^{\infty}(2n)\,f_e,\ \sum_{m=1}^{\infty} mf_{ei},\ \sum_{k=0,2,4,6}^{\infty} f_h \pm kf_e$
Stage II	$\sum_{k=0,2,4,6}^{\infty} f_h \pm kf_e$
Stage III	$\sum_{k=0,2,4,6}^{\infty} \pm kf_e,\ \sum_{k=0,2,4,6}^{\infty} (2f_h \pm kf_e)$
Stage IV	$\pm kf_e; k \in \{2,4,6,8,...\}$

TABLE III
DESIGN PARAMETERS OF THE BAND-PASS FILTERS.

Filter	*Central Frequency (fc)*	*Passing Band (fb)*
BPF I	f_h	$f_e^* \times h \times i$
BPF II	$h \times f_e^*$	$k \times f_e^*$

feeding the PLL must be generated from a single input signal (one ADC reading from one microphone).

The mentioned BPFs have the following transfer function:

$$H_{BPF}(S) = C\frac{2\pi f_b S}{S^2 + (2\pi f_b)\,S + (2\pi f_c)^2} \qquad (15)$$

where C, f_b, and f_c are correspondingly the constant coefficient, passing-band, and central frequency of the filter. Due to the different frequency each filter is centered at, dissimilar parameters must be applied as provided in Table III. The filters are designed to be adaptive to the reference electrical frequency (f_e^*) and h represents the harmonic order of the radial force sidebands around the injected frequency. There are two tuning factors introduced to the filters parameters namely $1 \leq i \leq 10$ and $0 < k \leq \frac{h}{2}$ where, theoretically, the impact of both i and k can be neglected by replacing them with 1. Tunable values are chosen to bolster the filtering robustness against stochastic environmental noise and non-modelled real-time conditions causing small frequency drifts.

Choosing the injected frequency is a critical step in this method, even more important than that of the conventional current-based sensorless controls. The frequency selection procedure must satisfy the following criteria:

- The injected frequency must be chosen in a manner to be synthesized with a satisfactory resolution through the PWM process.
- The injected frequency must be located in a zone where there is no or very few resonance frequencies of the

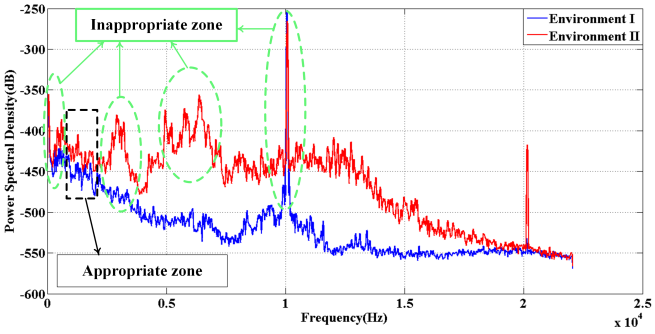

Fig. 5. Acoustic noise spectral comparison of the two usual environments our motor is working in.

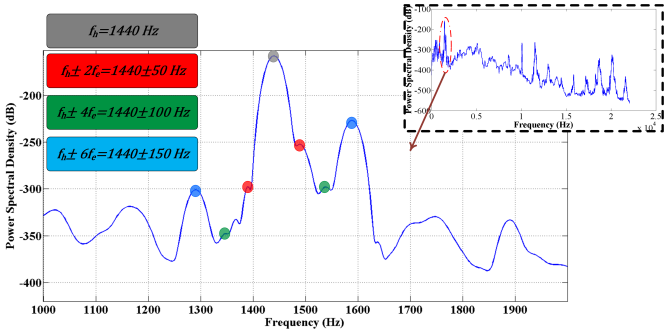

Fig. 6. Acoustic noise spectra at $500rpm$ and injection frequency of $1440Hz$.

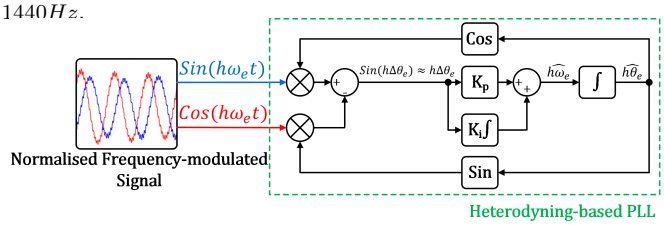

Fig. 7. Estimation of rotor speed and position through a heterodyning-based PLL fed by the processed radiated acoustic noise waveform.

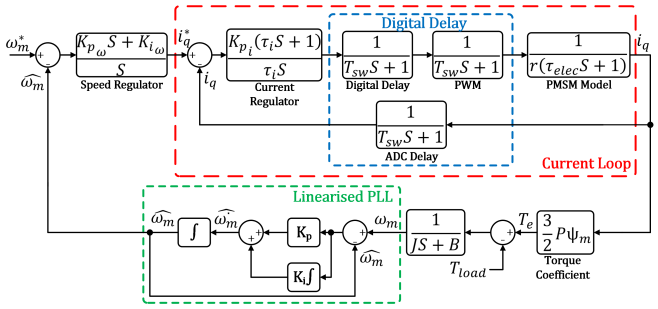

Fig. 8. Overall system block diagram considering current, observer, and speed loops.

structure. Acoustic noise spectrogram of the machine working without the injection should be used to identify the proper zone.

- The dominant sound of the environment where the machine is going to work in should be inspected to avoid any harmonic interference. In a multi-motor environment, like production lines, each motor disseminates one or several distinctive frequency component; consequently, the injection frequency should be used appropiately.

Having considered the above-mentioned criteria, the zone between $1000-2000Hz$ is the best zone for injection where $1440Hz$ is chosen. Figure (5) draws a comparison among the acoustic noise spectra for two different environment where the machine is usually working in. As observed, there is a tangible difference among the background sounds of the two environments with inappropriate zones with high amplitudes identified. On the other hand, the appropriate zone with relatively low amplitudes located within $1000-2000Hz$ is shown. The peak having the highest amplitude in both environments is occurred at $10KHz$ which is the switching frequency of the inverter and is not heard by the human ear. As a result, even the zones beyound the human audible capacity must be taken into consideration in order to make sure there is no unwanted interference.

For a condition where the signal is injected at $1440Hz$ and the motor is running at $500rpm$, the enlarged zone around the injected frequency in addition to the original spectra are shown in Fig. (6). As discussed earlier, there is a component at the injected frequency in addition to several speed-related sidebands where the three most dominant pairs are identified and shown.

Given Fig.(4), the orthogonal signals obtained at the output of the second BPF might have any arbitrary amplitude ($A.Sin(\omega_h t)$ and $A.Cos(\omega_h t)$ with A being the arbitrary amplitude); therefore, it is necessary to adopt a normalisaztion algorithm to make sure the amplitude is always unity and the performance will be independent of amplitude variations.

Finally, a heterodyning-driven PLL is fed by the normalised acquired space phasor from the second BPF to provide estimated values of the rotor position ($\hat{\theta}_e$) and speed ($\hat{\omega}_e$) as shown in Fig. (7). For the PLL structure, a PI-tracker meets the estimation requirements, even though it is possible to use more sophisticated structures with higher-order transfer functions.

B. Design of control loops and stability analysis

As shown in Fig. (8), the overall block diagram of a sensorless PMSM drive is composed of three main loops; the current, observer, and speed. The current loop model is comprised of a PI regulator, the machine electrical model, and the digital delays taking into account the impact of the code interrupt service routines (ISR), PWM strategy of the inverter and the ADC readings all having the value of $T_{sw} = 1/f_s$ where f_{sw} is the switching frequency (it is a common practice to synchronize all the ISRs and ADC readings with the PWM carrier waveform).

Taking into account the forward-path transfer function of the current loop

$$G_{i_{frw}} = \frac{K_{p_i}\left(\tau_i S+1\right)}{\tau_i S} \cdot \frac{1}{\underbrace{3T_{sw}}_{T_i} S+1} \cdot \frac{1}{r\left(\tau_{elec} S+1\right)} \tag{16}$$

the impact of the slowest pole related to the machine model near to the imaginary axis must be counteracted with the zero of the regulator, so

$$\tau_i = \tau_{elec} = \frac{L_q}{r} \tag{17}$$

where K_{p_i}, τ_i, and τ_{elec} denote the proportional gain of the current regulator, time constant of the current regulator and the time constant of the PMSM. Given (16,17), the closed loop transfer function of the current loop is derived as follows

$$G_{i_{cl}} = \frac{1}{1-T_{sw}S}.\frac{1}{2T_i^2S^2+2T_iS+1} \approx \frac{1}{\underbrace{(2T_i-T_{sw})}_{T_{eq_i}}S+1} \tag{18}$$

In derivation of (18), the term $2T_i^2S^2$ is neglected due to its smaller magnitude compared to the other terms. Consequently, the current loop can be replaced by a first-order delay element with the time constant equal to T_{eq_i}.

Considering the steady-state condition in which the error between the actual and estimated values is small enough, the PLL structure shown in Fig. (7) can be linearised, with the valid approximation of $Sin(h\Delta\theta_e) \approx h\Delta\theta_e$, to have the closed-loop transfer function of

$$G_{PLL} = \frac{\hat{\omega}}{\omega} = \frac{S.\hat{\theta}}{S.\theta} = \frac{K_pS+K_i}{S^2+K_pS+K_i} \tag{19}$$

where K_p and K_i are proportional and integral gains of the built-in PI in the PLL structure. Since the PLL is replaced by the conventional position sensor, definable by a simple delay element, its stable design is a determining factor affecting the whole system performance; therefore, given the input signals to the PLL having the frequency of ω_n, the parameters can be tuned as for a general second-order system with the damping ratio of ζ and undamped natural frequency of ω_n.

$$\frac{K_pS+K_i}{S^2+K_pS+K_i} \triangleq \frac{2\xi\omega_nS+\omega_n^2}{S^2+2\xi\omega_nS+\omega_n^2} \tag{20}$$

$$\begin{cases} K_p \triangleq 2\xi\omega_n \\ K_i \triangleq \omega_n^2 \end{cases} \tag{21}$$

Having modelled the current and observer loops, the forward transfer function of the speed loop is obtained as

$$G_{\omega_{frw}} = G_{PLL}.\frac{K_{p_\omega}S+K_{i_w}}{S}.\frac{1}{T_{eq_i}S+1}.\frac{3}{2}P\psi_m.\frac{1}{JS+B} \tag{22}$$

with K_{p_ω}, K_{i_ω}, J, and B respectively being the speed regulator PI parameters, shaft moment of inertia, and frictional losses. The system block diagram schematic is depicted in Fig. (8) where the load torque, T_{load}, is added as a disturbance. Bode diagram of the speed loop for three different revolution speeds of 50rpm, 300rpm, and 1000rpm is illustrated in Fig. (9) showing that, for all considered conditions, there are positive gain and phase margins leading to the closed-loop stability. The influence of introducing an observer to the system yields the occurrence of a bandwidth cap; for example for the goal frequency of 15Hz, the stable region falls between 5.76Hz and 69.3Hz or for the frequency of 300Hz the stable region is within the range of 5.76Hz and 354Hz showing that for each frequency, the system is stable but only in a limited frequency range. Consequently, as the speed reference changes, the goal frequency varies and accordingly the parameters of the obsever must be adapted to provide the system with a stable operation.

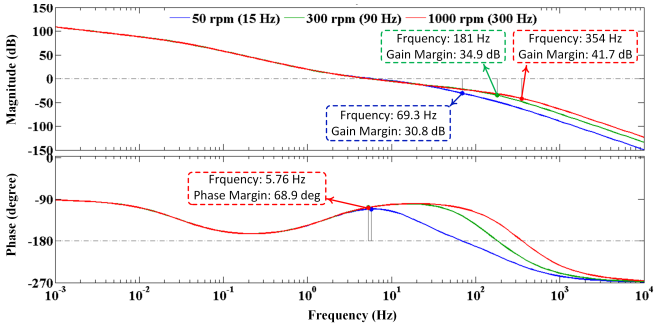

Fig. 9. Speed loop bode diagram.

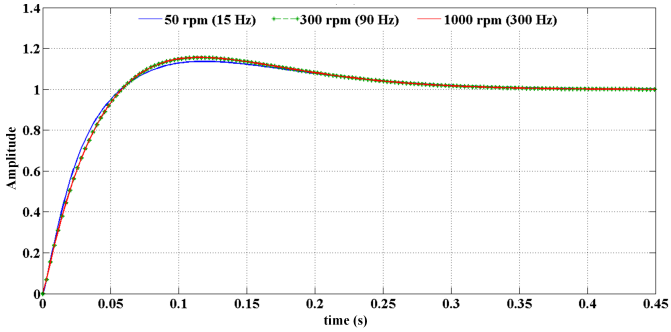

Fig. 10. Step response of the speed loop.

In addition, given the closed-loop transfer function of the speed loop

$$G_{\omega_{cl}} = \frac{1}{G_{PLL}}.\frac{G_{\omega_{frw}}}{1+G_{\omega_{frw}}} \tag{23}$$

the system step responses for the mentioned speeds are provided in Fig. (10) verifying the overally stable behaviour of the system; it is to be mentioned that the speed and current regulator parameters are kept constant while the observer parameters are tuned depending on the reference speed, yet the speed transients could be altered by changing the speed regulator parameters.

IV. Experimental Results

The proposed acoustic noise-based sensorless algorithm is experimentally verified on a test bench illustrated in Fig. (11) comprising a Texas Instrument DRV830X-HC-C2 kit (Inverter + TIF28069 DSP), two PMSMs with parameters summarized in Table.I (one acting as the motor and the other as the load), and a microphone with its dedicated signal conditioning circuits. It is to be mentioned that the field-oriented control is implemeted based on the estimated values of speed and position and the actual values obtained from the encoder are merely used for the the sake of comparison, $h = 6$ (providing a good SNR), the switching frequency of the inverter being the same with ADCs sampling rate is fixed at 10KHz, the maximum phase current of the motor is limited to 22A, and the applied DC link voltage is regulated at 50V.

A. Static conditions

Considering Fig. (12) for the low-speed reference value of 75rpm, the results for the actual and estimated rotor positions are compared where there exists a maximum position error of 0.606°. In addition, Fig. (13) draws a comparison among actual and estimated rotor positions for the speed of 1000rpm

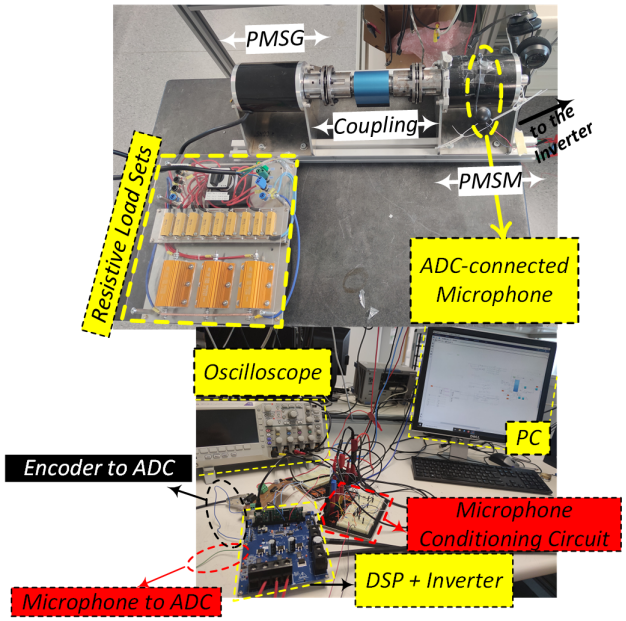

Fig. 11. Overview of the experimental setup.

while the position error is now increased to $3.3°$. The two post-processed signals feeding the PLL are correspondingly shown in Fig. (14) and Fig. (15) for the two mentioned speeds where the vertical cursors certify the signals orthogonality.

For the mechanical speeds of $75rpm$ and $1000rpm$, the mechanical frequencies are theoretically calculated as $1.25Hz$ and $16.67Hz$ respectively. Validating the accuracy of speed and position estimation, the frequencies of the obtained positions in Fig. (12) and Fig. (13) are accordingly $1.28Hz$ (2.4% error) and $16.83Hz$ (0.95% error).

According to (14), there are at least three dominant speed-related sidebands around the injected frequency (2^{nd}, 4^{th} and 6^{th} harmonics of the electrical frequency). Although each of these sidebands can be used for position estimation, the 6^{th} harmonic due to its better SNR is used in this article. For the two mentioned speeds, the 6^{th} harmonics have the following frequencies of $22.5Hz$ and $300Hz$ and these frequencies are experimentally acquired as $20.83Hz$ (7.42% error) and $306.748Hz$ (2.24% error) respectively (orthogonal waveforms shown in Fig.(14) and Fig. (15)). Consequently, it is quantitatively shown that as the speed increases, the existing error reduces.

Looking at the spectrogram shown in Fig. (3), it can be noticed that as the speed reaches $1000rpm$ (and above in a similar manner), the sidebands around the injected frequency and the low-frequency PM-related components approach each other. This closeness might culminate in component interference which shows itself as distortion in the estimated position like what is happened in Fig. (13). Such component interference can be avoided or postponed by increasing the injection frequency or increasing the injection amplitude or choosing another sideband for position estimation (changing the value of h).

B. Dynamic conditions

In order to accentuate the robustness of the proposed method, the drive performance is assessed in dynamic conditions including speed and load variations. The proposed method enables the machine to accurately perform in sudden speed reversals; figure (16) compares the actual and estimated rotor positions where the commanded speed has witnessed a step-wise transition from $+100$rpm to -100rpm while the maximum position error is $1.03°$.

The performance is also inspected in a condition where the

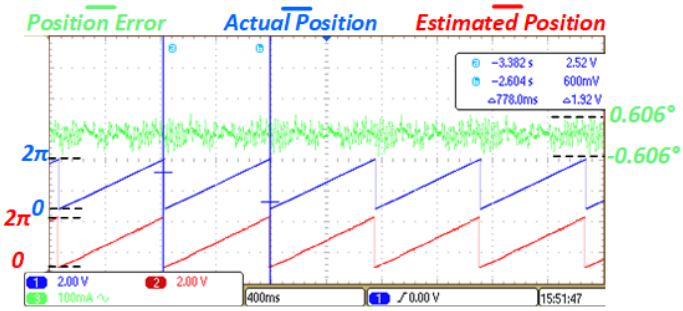

Fig. 12. Comparison of estimated and actual rotor positions at the reference speed of 75rpm.

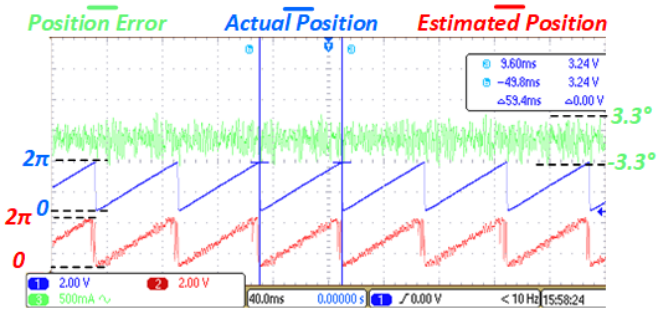

Fig. 13. Comparison of the estimated and actual rotor positions at the reference speed of 1000rpm.

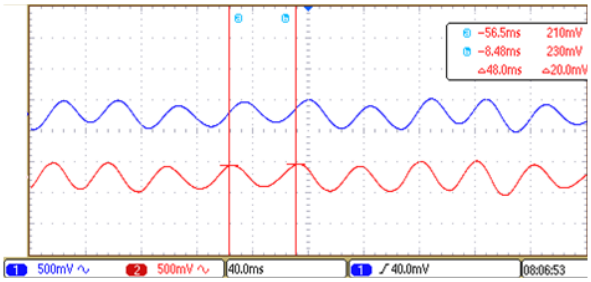

Fig. 14. Post-processed orthogonal signals acquired at the speed of 75rpm.

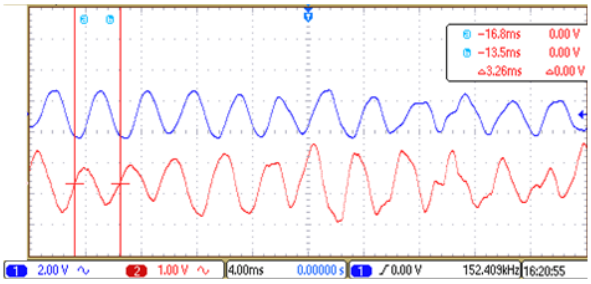

Fig. 15. Post-processed orthogonal signals acquired at the speed of 1000rpm.

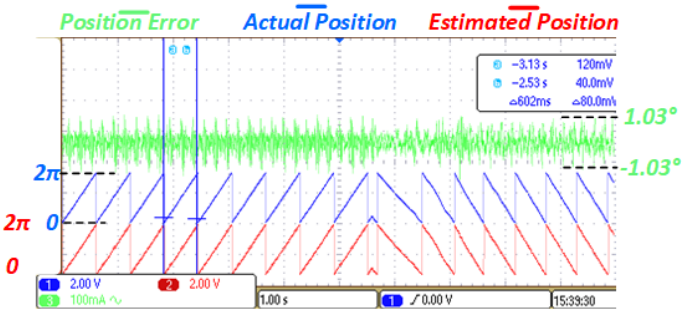

Fig. 16. Sensorless performance in sudden speed reversal ($\pm$100rpm).

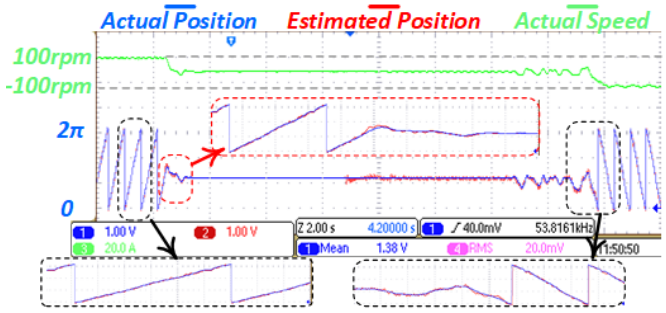

Fig. 17. Sensorless performance when speed changes from $100rpm$ to standstill and standstill to $-100rpm$.

speed is changed from $+100rpm$ to zero and then from zero to $-100rpm$ as shown in Fig. (17). Three instances are enlarged including steady-state at $100rpm$, entering into standstill from $100rpm$, and quitting standstill toward $-100rpm$. During all these instances, both the estimated and actual positions are perfectly following each other except for the instances of switching between rotation and standstill states with tiny differences among estimated and acctual positions.

Maintaining the same type of injection and observer structure, startup from standstill to $100rpm$ for NVH-based and conventional current-based sensorless controls are respectively illustrated in Fig.(18) and Fig.(19) for the purpose of comparison. Both methods have almost identical transient times (about three blocks of $1S$ time division) before the rotor starts to rotate for reaching the commanded speed which is directly due to the high inertia of the shaft. In terms of speed profile, the NVH-based method reaches the reference speed without any overshoot while there is an overshoot of about $50rpm$ (around 50% of the reference value) observed in the current-based sensorless method. Moreover, the estimated and actual positions perfectly follow each other in both methods.

Considering a situation in which the motor is normally operated with a position sensor, the NVH-based sensorless method can be a suitable reliability reserve when a sudden fault in the position sensor supervenes. This scenario can be simulated with an instant switch between the estimated and actual values (or vice versa) of speed and position in the control algorithm with results shown in Fig. (20). This test certifies the stability of the sensorless control since there is no difference observed in the performance of two conditions. The fundamental component of the phase current is also shown and it is observed that there is no change in its amplitude meaning that the position estimation is perfectly accomplished (otherwise, if there had been a difference between the actual and estimated d-axis positions, the amplitude of current would have changed when switched).

The system performance is studied when load variation in a fixed revolution speed occurs; since the load is composed of a PMSM connected to static resistors, the reference speed is set to a high value e.g. $500rpm$ providing enough EMF amplitude resulting in enough current in the resistors. Reflecting the load variations, q-axis current is also shown in Fig. (21). The load is composed of a tripple resistor configuration drawing $11A$ (36.7% of the nominal current), $13A$, and $22A$ (78.2% of the nominal current). During the load variations, the robust performance of our proposed method is verified as the speed profile successfully converges to the reference value at each instance of load step change. It is to be mentioned that the estimated and actual positions are perfectly synchronized as shown in the zoomed areas for the lowest and highest applied loads.

Another important aspect in a sensorless drive is its ability to withstand different speed commands; considering that and for the reference speed in the range of $100 - 500$rpm with increasing and decreasing changes, Fig. (22) depicts the speed profile affirming a satisfactory transient behaviour while the machine is connected to the resistor set resulting in the heaviest available load (the resistor set drawing $22A$ at $500rpm$). Estimated and actual positions are shown at two different speeds of $100rpm$ and $500rpm$ also. Nevertheless there is a ripple in the estimated position at $100rpm$ which can be attributed to the high inertia of the shaft for the low speed ranges, there is no phase shift between estimated and actual positions. It is worth mentioning that, as the speed increases, the ripple starts to disappear (comparing $100rpm$ and $500rpm$).

Throughout this section, successful steady-state performance of the proposed method in low and high speed conditions was shown. In addition, several dynamic conditions including speed reversal, operation at standstill, comparison of start-up between the proposed method and conventional current-based sensorless control, sudden switch among NVH-based and encoder-based controls, and load and speed variations were investigated and satisfactory performance of the NVH-based sensorless control was validated.

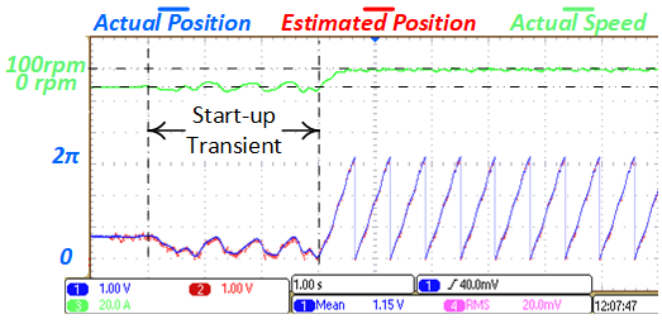

Fig. 18. Start-up performance in acoustic noise-based sensorless control.

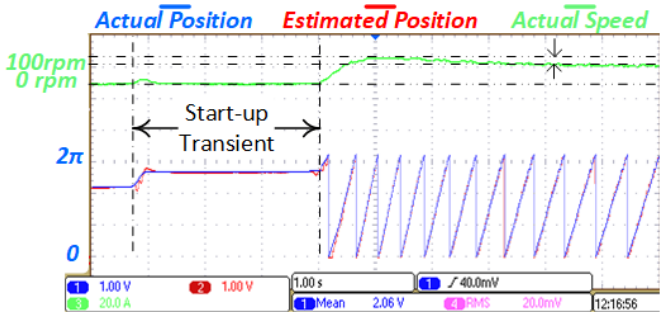

Fig. 19. Start-up performance in current-based sensorless control.

V. Conclusion

This article proposed a novel way to implement sensorless control of PMSM using its disseminated acoustic noise. Firstly, the underlying equations defining the formation of fields taking into account the impacts of PMs and current harmonics were provided. In the next stage, the impact of HFI method and its corresponding current harmonics on frequency composition of airgap fields and resulting radial forces were determined. Given a known injected frequency, it was validated that there would be several distinctive speed-related sidebands appeared in the acoustic noise spectra which could be used as the rotor position information source. Then, the signal processing stages in addition to the filtering design criteria alongside the whole speed-loop stability analysis were presented in details. Finally, the feasibility of an acoustic noise-based sensorless control for a given PMSM is experimentally verified and the system satisfactory performance is certified in different speeds and loading conditions.

References

[1] G. Abad, *Power electronics and electric drives for traction applications*. John Wiley & Sons, 2016.

[2] S. Morimoto, K. Kawamoto, M. Sanada, and Y. Takeda, "Sensorless control strategy for salient-pole pmsm based on extended emf in rotating reference frame," *IEEE transactions on industry applications*, vol. 38, no. 4, pp. 1054–1061, 2002.

[3] C. J. Volpato Filho, D. Xiao, R. P. Vieira, and A. Emadi, "Observers for high-speed sensorless pmsm drives: Design methods, tuning challenges and future trends," *IEEE Access*, vol. 9, pp. 56 397–56 415, 2021.

[4] G. Wang, M. Valla, and J. Solsona, "Position sensorless permanent magnet synchronous machine drivesâa review," *IEEE Transactions on Industrial Electronics*, vol. 67, no. 7, pp. 5830–5842, 2019.

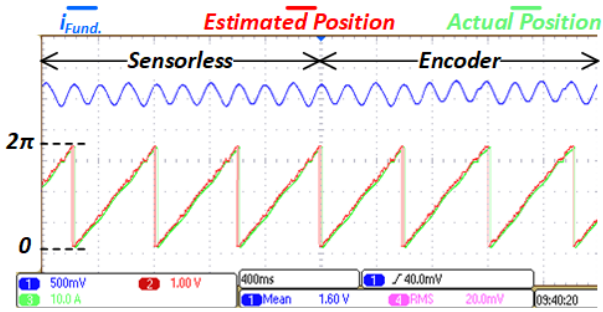

Fig. 20. Sudden switch among sensorless-based and encoder-based controls.

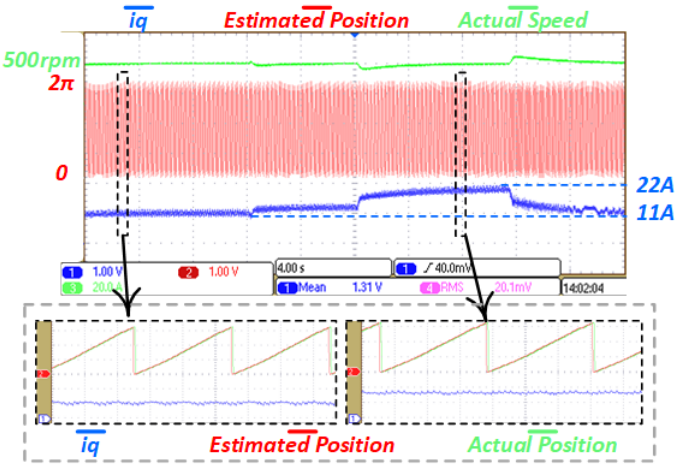

Fig. 21. Sensorless performance at 500rpm with load changes.

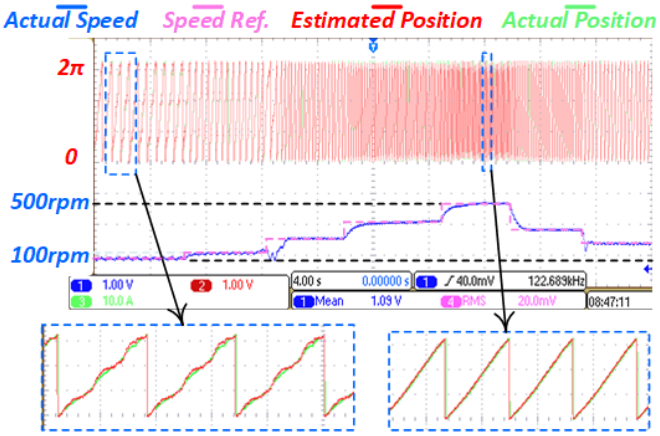

Fig. 22. Sensorless performance in the case of step-wise speed changes under heavy load.

[5] G. Zhu, A. Kaddouri, L.-A. Dessaint, and O. Akhrif, "A nonlinear state observer for the sensorless control of a permanent-magnet ac machine," *IEEE Transactions on Industrial Electronics*, vol. 48, no. 6, pp. 1098–1108, 2001.

[6] Y. Lee and S.-K. Sul, "Model-based sensorless control of an ipmsm with enhanced robustness against load disturbances based on position and speed estimator using a speed error," *IEEE Transactions on Industry Applications*, vol. 54, no. 2, pp. 1448–1459, 2017.

[7] Y. Zhang, Z. Yin, C. Bai, G. Wang, and J. Liu, "A rotor position and speed estimation method using an improved linear extended state observer for ipmsm sensorless drives," *IEEE Transactions on Power Electronics*, vol. 36, no. 12, pp. 14 062–14 073, 2021.

[8] T.-C. Lin, Z.-Q. Zhu, and J. Liu, "Improved rotor position estimation in sensorless-controlled permanent-magnet synchronous machines having asymmetric-emf with harmonic compensation," *IEEE Transactions on Industrial Electronics*, vol. 62, no. 10, pp. 6131–6139, 2015.

[9] X. Wu, Y. Feng, X. Liu, S. Huang, X. Yuan, J. Gao, and J. Zheng, "Initial rotor position detection for sensorless interior pmsm with square-wave voltage injection," *IEEE Transactions on Magnetics*, vol. 53, no. 11, pp. 1–4, 2017.

[10] V. C. Ilioudis, "Sensorless control of permanent magnet synchronous machine with magnetic saliency tracking based on voltage signal injection," *Machines*, vol. 8, no. 1, p. 14, 2020.

[11] N. Bianchi, S. Bolognani, J.-H. Jang, and S.-K. Sul, "Comparison of pm motor structures and sensorless control techniques for zero-speed rotor position detection," *IEEE transactions on power Electronics*, vol. 22, no. 6, pp. 2466–2475, 2007.

[12] X. Luo, Q. Tang, A. Shen, and Q. Zhang, "Pmsm sensorless control by injecting hf pulsating carrier signal into estimated fixed-frequency

rotating reference frame," *IEEE Transactions on Industrial Electronics*, vol. 63, no. 4, pp. 2294–2303, 2015.
[13] X. Zhang, H. Li, S. Yang, and M. Ma, "Improved initial rotor position estimation for pmsm drives based on hf pulsating voltage signal injection," *IEEE Transactions on Industrial Electronics*, vol. 65, no. 6, pp. 4702–4713, 2017.
[14] Q. Lu, Y. Wang, L. Mo, and T. Zhang, "Pulsating high frequency voltage injection strategy for sensorless permanent magnet synchronous motor drives," *IEEE Transactions on Applied Superconductivity*, vol. 31, no. 8, pp. 1–4, 2021.
[15] S. Golestan, M. Monfared, and J. M. Guerrero, "Second order generalized integrator based reference current generation method for single-phase shunt active power filters under adverse grid conditions," in *4th Annual International Power Electronics, Drive Systems and Technologies Conference*, pp. 510–517. IEEE, 2013.
[16] A. H. Almarhoon, Z. Zhu, and P. Xu, "Improved rotor position estimation accuracy by rotating carrier signal injection utilizing zero-sequence carrier voltage for dual three-phase pmsm," *IEEE Transactions on Industrial Electronics*, vol. 64, no. 6, pp. 4454–4462, 2016.
[17] M. Mamo, K. Ide, M. Sawamura, and J. Oyama, "Novel rotor position extraction based on carrier frequency component method (cfcm) using two reference frames for ipm drives," *IEEE Transactions on industrial electronics*, vol. 52, no. 2, pp. 508–514, 2005.
[18] M. Hofer, M. Nikowitz, and M. Schroedl, "Sensorless control of a reluctance synchronous machine in the whole speed range without voltage pulse injections," in *2017 IEEE 3rd International Future Energy Electronics Conference and ECCE Asia (IFEEC 2017-ECCE Asia)*, pp. 1194–1198. IEEE, 2017.
[19] X. Fu, Y. Xu, H. He, and X. Fu, "Initial rotor position estimation by detecting vibration of permanent magnet synchronous machine," *IEEE Transactions on Industrial Electronics*, vol. 68, no. 8, pp. 6595–6606, 2020.
[20] C. Lin, S. Wang, M. Moallem, B. Fahimi, and C. Tschida, "Analysis of vibration in permanent magnet synchronous machines due to variable speed drives," *IEEE Transactions on Energy Conversion*, vol. 32, no. 2, pp. 582–590, 2016.
[21] Z. Zhu, Z. P. Xia, L. Wu, and G. W. Jewell, "Analytical modeling and finite-element computation of radial vibration force in fractional-slot permanent-magnet brushless machines," *IEEE Transactions on Industry Applications*, vol. 46, no. 5, pp. 1908–1918, 2010.
[22] Z. Zhu, Z. Xia, L. Wu, and G. Jewell, "Influence of slot and pole number combination on radial force and vibration modes in fractional slot pm brushless machines having single-and double-layer windings," in *2009 IEEE Energy Conversion Congress and Exposition*, pp. 3443–3450. IEEE, 2009.
[23] J. F. Gieras, C. Wang, and J. C. Lai, *Noise of polyphase electric motors*. CRC press, 2018.
[24] F. Lin, S. Zuo, W. Deng, and S. Wu, "Modeling and analysis of electromagnetic force, vibration, and noise in permanent-magnet synchronous motor considering current harmonics," *IEEE Transactions on Industrial Electronics*, vol. 63, no. 12, pp. 7455–7466, 2016.

Amirhossein Malekipour (Graduate Student Member, IEEE) was born on August 15, 1993. He obtained his M.Sc degree with distinction in the field of electric machines and power electronics from the Isfahan University of Technology, Isfahan, Iran, in 2019. He is currently pursuing his Ph.D degree in electrical engineering at the University of Grenoble Alpes (UGA), Grenoble, France. His current research interests encompass design and digital control of electric drives and power electronics converters, sensorless control of electric machines, electric machines fault detection, and NVH analysis of electromechanical energy conversion systems.

Adrien Corne (Member, IEEE) received the Engineering degree in electrical engineering from the Ecole Nationale Supérieure d'Electricité et de Méchanique (ENSEM), Université de Lorraine, Nancy, France, in 2014 and the Ph.D degree in electrical engineering from the Université de Lorraine in 2019. His research interests include sensorless control of electrical machines, nonlinear and robust observers for electrical systems, machine parametric sensitivity analysis, and electric machines fault detection.

Lauric Garbuio (Member, IEEE) received his M.Sc degree from The École Normale Supérieure Paris-Saclay, Paris, France in 2001 and the Ph.D degree in electrical engineering in 2006 from the Institut National Polytechnique de Toulouse, Tolouse, France. Since 2010, he has been with the Grenoble Electrical Engineering Laboratory (G2Elab) of the University of Grenoble Alpes (UGA) as an associate professor. His current research interests include the modeling and conception of innovative electrical systems for power generation and transportation systems.

Pierre Granjon was born in France in 1971. He received the Ph.D degree in signal processing from the the University of Grenoble Alpes (UGA), France, in 2000. He joined the laboratory of image and signal processing of the GIPSA-Lab, University of Grenoble Alpes in 2007 as an associate professor. He has developed several monitoring methods for electrical rotating machines and power networks based on the analysis of vibration or electrical parameters. His current research is mainly focused on developing efficient methods to properly analyze three-component signals such as three-axis vibration or three-phase electrical quantities.

Laurent Gerbaud (Member, IEEE) received the Ph.D degree in electrical engineering from the University of Grenoble Alpes, Grenoble, France, in 1993. He was successively a researcher, assistant professor, and now professor at the Grenoble Electrical Engineering Laboratory (G2Elab) of the University of Grenoble ALpes (UGA) and CNRS. His research interests include electrical drives and power electronics applications.